Simulation of the SuperSAR Multi-Azimuth Synthetic Aperture Radar Imaging System for Precise Measurement of Three-Dimensional Earth Surface Displacement

Hyung-Sup Jung, *Member, IEEE*, Zhong Lu, Andrew Shepherd, and Tim Wright

***Abstract*—The SuperSAR imaging system, a novel multi-azimuth synthetic aperture radar (SAR) system capable of detecting Earth surface deformation in three dimensions from a single satellite platform, has recently been proposed. In this paper, we investigate the feasibility of detecting precise 3-D surface displacement measurements with the SuperSAR imaging system using a point target simulation. From this simulation, we establish both a relationship between the interferometric SAR phase and the across-track displacement and a relationship between the multiple-aperture interferometry phase and the along-track displacement based on the SuperSAR imaging geometry. The theoretical uncertainties of the SuperSAR measurement are analyzed in the across- and along-track directions, and the theoretical accuracy of the 3-D displacement measurement from the SuperSAR system is also investigated according to both the decorrelation and the squint and look angles. In the case that the interferometric coherence is about 0.8 and that five effective looks are employed, the theoretical 2-D measurement precision values are about 3.67 and 6.35 mm in the across- and along-track directions, respectively, and the theoretical 3-D measurement precision values for 3-D displacement are about 4.05, 4.56, and 3.45 mm in the east, north, and up directions, respectively. The result of this study demonstrates that the SuperSAR imaging system is capable of measuring the 3-D surface displacement in all directions with subcentimeter precision.**

***Index Terms*—Interferometric synthetic aperture radar (InSAR), multiple-aperture interferometry (MAI), squint SAR, SuperSAR.**

Manuscript received June 19, 2014; revised January 12, 2015 and April 10, 2015; accepted May 2, 2015. This work was supported in part by the "Development of Geostationary Meteorological Satellite Ground Segment" (NMSC-2014-01) program funded by the National Meteorological Satellite Centre of the Korea Meteorological Administration and in part by the Space Core Technology Development Program through the National Research Foundation of Korea funded by the Ministry of Education, Science and Technology under Grant 2012M1A3A3A02033465.

H.-S. Jung is with the Department of Geoinformatics, The University of Seoul, Seoul 130-743, Korea (e-mail: hsjung@uos.ac.kr).

Z. Lu was with the Cascades Volcano Observatory, U.S. Geological Survey, Vancouver, WA 98683 USA. He is now with the Huffington Department of Earth Sciences, Southern Methodist University, Dallas, TX 75275 USA.

A. Shepherd and T. Wright are with the School of Earth and Environment, University of Leeds, Leeds LS2 9JT, U.K.

Color versions of one or more of the figures in this paper are available online at http://ieeexplore.ieee.org.

Digital Object Identifier 10.1109/TGRS.2015.2435776

I. Introduction

SYNTHETIC aperture radar (SAR) interferometry (InSAR) is a powerful technique for mapping Earth surface displacements with meter- to decameter-scale spatial resolution and with millimeter to centimeter measurement accuracy over large areas (up to thousands of square kilometers). The InSAR method has been successfully used for investigating many signals of Earth surface deformation, including earthquakes [1]–[3], volcanic activities [4]–[8], landslides [9]–[11], ground subsidence [12]–[15], and glacier ice estimation [16]–[18]. However, the InSAR imaging geometry is allowed to only measure surface displacements in the line-of-sight (LOS) direction, which is toward or away from the satellite.

The combination of multiple InSAR measurements from ascending and descending orbits enables us to retrieve 2-D displacements composed of both the ground range and up components but cannot measure the along-track component. For this reason, it is almost impossible for this method to measure a precise 3-D surface displacement. The measurement of 3-D surface displacement is essential for resolving model parameters from earthquakes and volcanic activity, but neither the conventional InSAR nor its combination methods can resolve the model parameters because there is a marked tradeoff among the model parameters [4], [19].

Attempts to retrieve 3-D surface displacement data have included the following methods using 1) azimuth offset fields created by cross correlation of SAR amplitude images [20]–[23], 2) interferograms with different viewing geometries (ascending and descending, left and right looking, different look angles) [19], [24], and 3) a combination of the InSAR and Global Positioning System measurements [25]–[29]. The former method is more suitable for estimating the north component of large displacements that cause a significant decorrelation in the InSAR technique rather than small displacements. The latter technique also has largely reduced accuracy in the north component at most areas except the polar regions because conventional interferograms are created by using data acquired on near-polar orbiting satellites. This issue results from the inherent difficulty of measuring displacements in the along-track direction.

Bechor and Zebker [30] have developed a multiple-aperture SAR interferometry (MAI) technique that achieves remarkable improvement in along-track displacement measurements. This

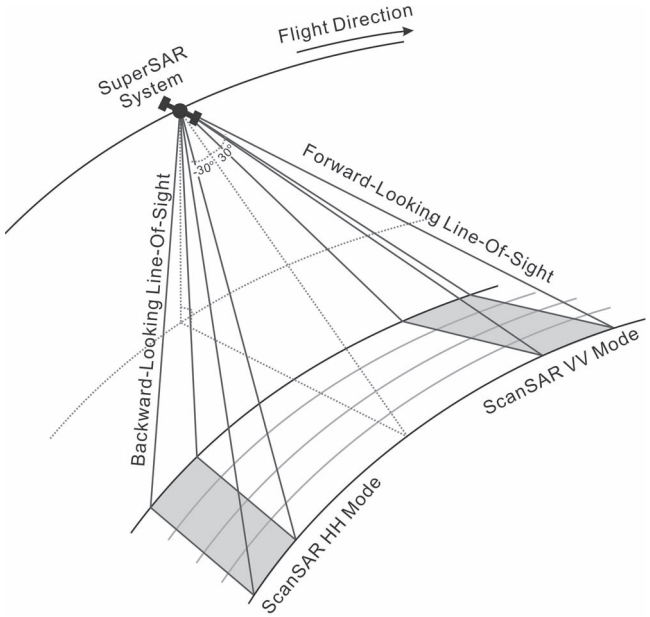

Fig. 1. SuperSAR imaging geometry. The SuperSAR system is an L-band ScanSAR that can simultaneously acquire two SAR images from forward- and backward-looking beams.

method can measure the along-track displacement with measurement accuracy of several centimeters using a MAI interferogram created by the forward- and backward-looking interferograms using sub-aperture InSAR processing. Jung *et al.* [31]–[33] have proposed a further improved method of MAI processing, which is designed to enhance interferometric coherence and correct phase contributions from the flat-Earth and topographic effects. The phase contributions are caused by the perpendicular baseline difference between forward- and backward-looking interferograms. This MAI method has been successfully combined with conventional InSAR methods to retrieve a 3-D surface deformation. In addition, this method has been used to correct an ionosphere-distorted SAR interferogram [34], [35].

Although centimeter-level accuracy can be achieved by the MAI technique, it is much lower than the millimeter-level accuracy of the conventional InSAR. The discrepancy of accuracy values between LOS and along-track displacements measured from InSAR and MAI methods is not allowed to retrieve perfect 3-D surface displacements. To surmount this limitation, the SuperSAR imaging system has been proposed, which is a novel multi-azimuth SAR system that is capable of detecting Earth surface deformation in three dimensions [36], [37]. Using InSAR and MAI, this system is capable of simultaneously measuring surface displacement perpendicular and parallel, respectively, to the satellite ground track. As shown in Fig. 1, the SuperSAR system can obtain forward- and backward-looking SAR images simultaneously. Thus, key elements in the design of the sensor are to generate multiple beam, which is achieved through phased-array antenna. SuperSAR is an L-band ScanSAR system having the wavelength of about 23.8 cm and acquires the VV- and HH-polarized SAR images from forward- and backward-looking beams, respectively. Thus, the phase center of each polarization would not be different because each beam does not illuminate the same scatterer. The incidence angle of SuperSAR are in the range of about 30° and 50°, and the squint angles of SuperSAR are in about 30° and −30° in forward- and backward-looking directions, respectively. The revisit time of the SuperSAR system is 13 days. In order to monitor all actively deforming regions, the importance of obtaining measurements in three dimensions has been highlighted. Only SuperSAR system has the ability to achieve 1 mm/year accuracy over 100 km in all three dimensions after five years of observation [37]. Consequently, the SuperSAR is allowed to map strain accumulating around faults that are responsible for 95% of damaging onshore earthquakes.

In this paper, we simulate the SuperSAR imaging system for performance analysis of 3-D surface displacement measurement. For the mathematical derivations of the SuperSAR measurements, we establish the following: a relationship between the InSAR phase and the across-track displacement and a relationship between the MAI phase and the along-track displacement from the SuperSAR imaging geometry. Moreover, the theoretical uncertainties of the SuperSAR measurement are analyzed in the across- and along-track directions, and the theoretical accuracy of 3-D displacement measurement from the SuperSAR system is also investigated according to both the decorrelation and the squint and look angles. For analysis of the SuperSAR system measurement performance, the raw data are simulated to provide a static point target. From this simulation, it is demonstrated that the SuperSAR imaging system can measure 2-D and 3-D surface displacements with subcentimeter precision in all directions.

II. Methods

The SuperSAR is a novel multi-azimuth SAR system that is able to detect precise Earth surface deformation in three dimensions. This system can obtain forward- and backward-looking SAR images simultaneously from the squint angles of about 30° and −30°. On the contrary, the conventional SAR systems get a single SAR image, and then, the forward- and backward-looking SAR images are generated by means of split-beam SAR processing. Hence, its squint angle is very small, and the measured surface displacement parallel to the satellite ground track has very low accuracy compared with the one perpendicular to the satellite ground track. Unlike the conventional SAR systems, the SuperSAR system can measure precise surface displacements perpendicular and parallel to the satellite ground track simultaneously due to the large difference between the squint angles of the forward- and backward-looking SAR images.

In this section, we establish 1) a relationship between the InSAR phase and the across-track displacement and 2) a relationship between the MAI phase and the along-track displacement from the SuperSAR imaging geometry. Additionally, theoretical measurement uncertainties of the across- and along-track displacements are analyzed. Moreover, the theoretical accuracy of the 3-D displacement measurement is derived with respect to both the decorrelation and the squint and look angles.

A. Point Scatterer Response for Squint-Mode SAR

The response from a static point scatterer located at slant range r_s and azimuth time $t = 0$ for an azimuth antenna weighting

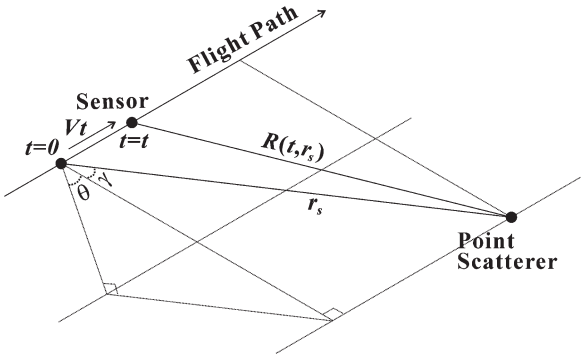

Fig. 2. Squint SAR data acquisition geometry for the SuperSAR imaging system.

$a(\cdot)$ with transmitted signal envelope $s_0(\cdot)$ is given by the following equation [38], [39]:

$$s(\tau,t;r_s)=a(t;r_s)\cdot s_0\left(\tau-\frac{2R(t;r_s)}{c}\right)\cdot\exp\left(-i\frac{4\pi}{\lambda}R(t;r_s)\right) \quad (1)$$

where t is the time along the radar flight path, τ is the delay time in the slant-range direction, c is the speed of light, and λ is the radar wavelength (see Fig. 2). The transmitted signal is

$$s_0\left(\tau-\frac{2R(t;r_s)}{c}\right)=\exp\left[i\pi k\left(\tau-\frac{2R(t;r_s)}{c}\right)^2\right] \quad (2)$$

where k is the chirp slope, and the time-varying distance from the radar to the scatterer is given by

$$R(t;r_s)=\sqrt{r_s^2+V(r_s)^2t^2-2r_sV(r_s)t\sin\gamma(r_s)} \quad (3)$$

where $V(r_s)$ and $\gamma(r_s)$ are the range-dependent effective platform velocity and squint angle, respectively (see Fig. 2).

Using a Taylor expansion, the slant-range distance can be approximated by

$$R(t;r_s)\approx r_s-V(r_s)\sin\gamma(r_s)\cdot t+\frac{V(r_s)^2\cos^2\gamma(r_s)}{r_s}\cdot\frac{t^2}{2}. \quad (4)$$

The phase of the return signal can then be written as follows:

$$\begin{aligned}\phi(t)&=\exp\left(-i\frac{4\pi}{\lambda}R(t;r_s)\right)\\&=\exp\left\{-i\frac{4\pi}{\lambda}r_s\right\}\\&\quad\times\exp\left\{i2\pi\left(\frac{2V(r_s)\sin\gamma(r_s)}{\lambda}\cdot t-\frac{2V(r_s)^2\cos^2\gamma(r_s)}{\lambda r_s}\cdot\frac{t^2}{2}\right)\right\}\\&=\exp\left\{-i\frac{4\pi}{\lambda}r_s\right\}\exp\left\{i2\pi\left(f_{\rm DC}(r_s)\cdot t+f_R(r_s)\cdot\frac{t^2}{2}\right)\right\}\end{aligned} \quad (5)$$

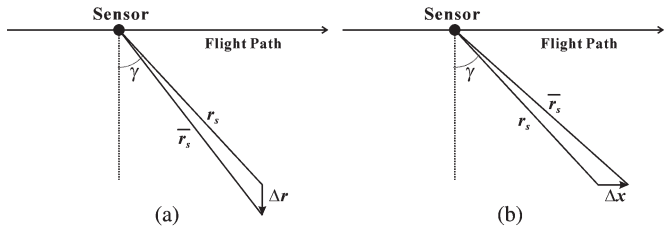

Fig. 3. Variation in the slant-range distance with respect to the across-track displacement (Δr) and the along-track displacement (Δx).

where $f_{\rm DC}$ is the Doppler centroid, and f_R is the Doppler rate. Based on (5), we can define the squint angle from the Doppler centroid as follows:

$$\gamma(r_s)=\sin^{-1}\left(\frac{\lambda}{2V(r_s)}f_{\rm DC}(r_s)\right). \quad (6)$$

The azimuth resolution $R_{\rm az}$ is defined from (5) as

$$R_{\rm az}\approx\frac{l}{2\cos^2\gamma} \quad (7)$$

where l is the effective azimuth antenna length.

B. Measurement of 2-D Displacement

Fig. 3 shows the across-track (Δr) and along-track (Δx) components of the slant-range displacement from the SuperSAR forward-looking data acquisition geometry. As shown in Fig. 3(a), slant-range distance $\bar{r}_s(\Delta r)$ [including the across-track displacement (Δr)] can be defined using the law of cosines and is given by

$$\bar{r}_s(\Delta r)=\sqrt{r_s^2+\Delta r^2+2\Delta r\cdot r_s\cos\gamma}. \quad (8)$$

The Taylor expansion of (8) is

$$\bar{r}_s(\Delta r)=r_s+\cos\gamma\cdot\Delta r+\frac{\sin^2\gamma}{r_s}\cdot(\Delta r)^2+\cdots. \quad (9)$$

For the SuperSAR system, the value of $\sin^2\gamma/r_s$ is 3.94×10^{-7} m^{-1} when $\gamma=30^\circ$. and $r_s=635$ km. Thus, we can assume $\sin^2\gamma/r_s\approx0$, and then, $\bar{r}_s(\Delta r)$ can be approximated as

$$\bar{r}_s(\Delta r)\approx r_s+\cos\gamma\cdot\Delta r. \quad (10)$$

Slant-range distance $\bar{r}_s(\Delta x)$ [including the along-track displacement (Δx)] can also be approximated as follows [as shown in Fig. 3(b)]:

$$\bar{r}_s(\Delta x)\approx r_s+\sin\gamma\cdot\Delta x \quad (11)$$

where the approximation enables us to assume $\cos^2\gamma/r_s=1.2\times10^{-6}$ m^{-1} as zero. Obtained from the squint SAR geometry, interferometric phase $\Delta\phi$ can be defined by

$$\Delta\phi=-\frac{4\pi}{\lambda}(\bar{r}_s-r_s) \quad (12)$$

where r_s and $\bar{r}_s$ are the slant-range distances of the master and slave SAR acquisitions, respectively. If the across- and

along-track components of the slant-range displacement are assumed, $\Delta\phi$ can be rewritten as

$$\Delta\phi = \frac{4\pi}{\lambda}(\delta\rho + \Delta r\cos\gamma + \Delta x\sin\gamma) \tag{13}$$

where $\delta\rho$ is the slant-range difference caused by the baseline B defined as [40]

$$\delta\rho = -B\sin(\theta - \alpha) \tag{14}$$

where B is the baseline, and θ and α are the look angle and baseline orientation, respectively. $\delta\rho$ relates to the flat-Earth and topographic phases.

Phases $\Delta\phi_f$ and $\Delta\phi_b$ of the forward- and backward-looking interferograms can be defined as

$$\Delta\phi_f = \frac{4\pi}{\lambda}\left[-B_f\sin(\theta_f - \alpha_f) + \Delta r\cos\gamma_f + \Delta x\sin\gamma_f\right] \tag{15}$$

$$\Delta\phi_b = \frac{4\pi}{\lambda}\left[-(B_f + \Delta B)\cdot\sin(\theta_f - \alpha_f + \Delta\theta - \Delta\alpha) + \Delta r\cos\gamma_b + \Delta x\sin\gamma_b\right] \tag{16}$$

where B_f, θ_f, α_f, and γ_f are the baseline, look angle, baseline orientation, and squint angle of forward-looking acquisition, respectively; γ_b is the squint angle of backward-looking acquisition; and ΔB, $\Delta\theta$, and $\Delta\alpha$ are the differences in the baseline, look angle, and baseline orientation, respectively, between the forward- and backward-looking pairs. For spaceborne SAR systems, if the absolute values of the Doppler centroids for the forward- and backward-looking acquisitions are similar, the look-angle difference would be small; consequently, $|\Delta\theta - \Delta\alpha|$ is negligible. $\Delta\phi_b$ can then be approximated as

$$\Delta\phi_b = \frac{4\pi}{\lambda}\left[-(B_f + \Delta B)\cdot\sin(\theta_f - \alpha_f) + \Delta r\cos\gamma_b + \Delta x\sin\gamma_b\right]. \tag{17}$$

InSAR phase ϕ_{InSAR} is defined by adding the phases of the forward- and backward-looking interferograms, as given by

$$\begin{aligned}\phi_{\mathrm{InSAR}} &= \frac{\Delta\phi_f + \Delta\phi_b}{2} \\ &= \frac{4\pi}{\lambda}\left[-\left(B_f + \frac{\Delta B}{2}\right)\sin(\theta_f - \alpha_f) + \frac{\Delta r(\cos\gamma_f + \cos\gamma_b)}{2} + \frac{\Delta x(\sin\gamma_f + \sin\gamma_b)}{2}\right].\end{aligned} \tag{18}$$

If the absolute values of the Doppler centroids for the forward- and backward-looking acquisitions are similar, $\gamma_f + \gamma_b$ will be approximately 0, and phase ϕ_{InSAR} can then be approximated as

$$\phi_{\mathrm{InSAR}} \approx \frac{4\pi}{\lambda}\left[-\left(B_f + \frac{\Delta B}{2}\right)\sin(\theta_f - \alpha_f) + \Delta r\cos\left(\frac{\gamma_f - \gamma_b}{2}\right)\right]. \tag{19}$$

After correcting the flat-Earth and topographic phases for the baseline and baseline difference, across-track displacement Δr can be defined by

$$\Delta r = \frac{\lambda}{\cos\left(\frac{\gamma_f - \gamma_b}{2}\right)}\frac{\phi_{\mathrm{InSAR}}}{4\pi} \tag{20}$$

and rewritten as

$$\Delta r = \lambda_s\cdot\frac{\phi_{\mathrm{InSAR}}}{4\pi} \tag{21}$$

where λ_s is the adjusted radar wavelength, which is defined using (6) as follows:

$$\lambda_s = \frac{\lambda}{\sqrt{1 - \frac{\lambda^2}{4\Delta_{\mathrm{az}}^2}n_{\mathrm{dop}}^2}} \tag{22}$$

where Δ_{az} is the azimuth cell spacing, which is defined as V/PRF, where PRF is the pulse repetition frequency. n_{dop}^2 is defined by

$$n_{\mathrm{dop}}^2 = -n_{\mathrm{dop},f}\cdot n_{\mathrm{dop},b} \tag{23}$$

where $n_{\mathrm{dop},f}$ and $n_{\mathrm{dop},b}$ are the Doppler ambiguity numbers of forward- and backward-looking acquisitions, which are represented by real values (and not integers) and are defined as

$$n_{\mathrm{dop},f} = \frac{f_{\mathrm{DC},f}}{\mathrm{PRF}} \qquad n_{\mathrm{dop},b} = \frac{f_{\mathrm{DC},b}}{\mathrm{PRF}}. \tag{24}$$

MAI phase ϕ_{MAI} can be defined by subtracting the phases of the forward- and backward-looking interferograms, as given by

$$\begin{aligned}\phi_{\mathrm{MAI}} &= \Delta\phi_f - \Delta\phi_b \\ &= \frac{4\pi}{\lambda}\left[\Delta B\sin(\theta_f - \alpha_f) + \Delta r(\cos\gamma_f - \cos\gamma_b) + \Delta x(\sin\gamma_f - \sin\gamma_b)\right]\end{aligned} \tag{25}$$

and approximated by

$$\phi_{\mathrm{MAI}} \approx \frac{4\pi}{\lambda}\left[\Delta B\sin(\theta_f - \alpha_f) + \Delta x(\sin\gamma_f - \sin\gamma_b)\right]. \tag{26}$$

After correcting the flat-Earth and topographic phases for the baseline and baseline difference, the along-track displacement can be defined as

$$\Delta x = \frac{\lambda}{\sin\gamma_f - \sin\gamma_b}\cdot\frac{\phi_{\mathrm{MAI}}}{4\pi} = \frac{2V}{f_{\mathrm{DC},f} - f_{\mathrm{DC},b}}\cdot\frac{\phi_{\mathrm{MAI}}}{4\pi} \tag{27}$$

and can be rewritten using (4) as follows:

$$\Delta x = l_s\cdot\frac{\phi_{\mathrm{MAI}}}{2\pi} \tag{28}$$

where l_s is the adjusted synthetic antenna length for squint SAR geometry, which is defined by

$$l_s = \frac{\Delta_{\mathrm{az}}}{\Delta n_{\mathrm{dop}}} \tag{29}$$

where Δn_{dop} is defined by $n_{\mathrm{dop},f} - n_{\mathrm{dop},b}$.

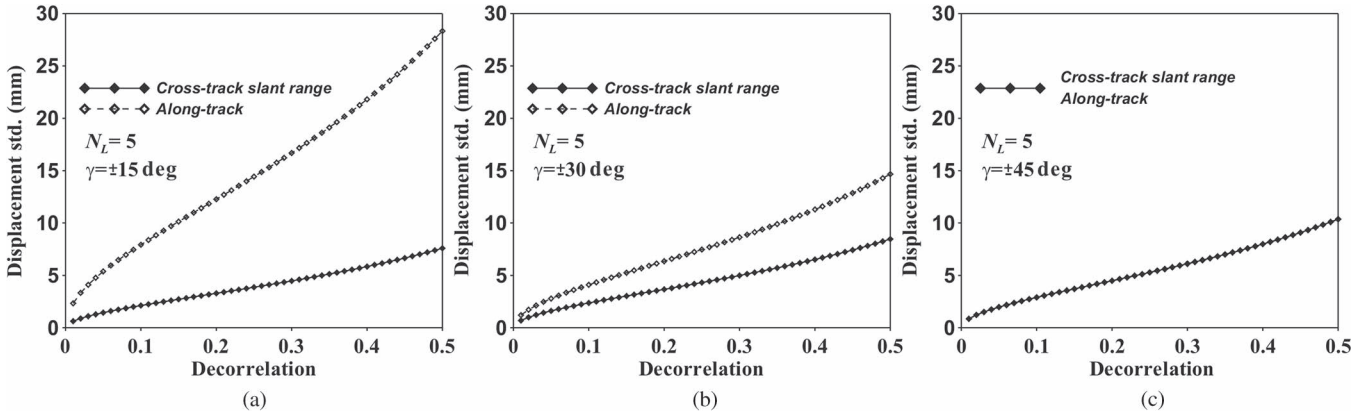

Fig. 4. Variation in the standard deviations of across- and along-track displacements with respect to decorrelation using squint angles of (a) 15°, (b) 30°, and (c) 45°, where parameters of $V = 7589$ m/s, PRF $= 2300$ Hz, and $\lambda = 23.79$ cm are used.

C. Measurement Uncertainty of 2-D Displacement

Measurement uncertainty of the across-track displacement (σ_r) can be calculated from (21) as

$$\sigma_r = \frac{\lambda_s}{4\pi} \cdot \sigma_{\phi,\mathrm{InSAR}} \tag{30}$$

where $\sigma_{\phi,\mathrm{InSAR}}$ is the standard deviation of the SuperSAR's InSAR phase. The measurement uncertainty of the along-track displacement (σ_x) is also calculated from (28) and is given by

$$\sigma_x = \frac{l_s}{2\pi} \cdot \sigma_{\phi,\mathrm{MAI}} \tag{31}$$

where $\sigma_{\phi,\mathrm{MAI}}$ is the standard deviation of the SuperSAR's MAI phase.

The standard deviations of $\sigma_{\phi,\mathrm{InSAR}}$ and $\sigma_{\phi,\mathrm{MAI}}$ can be defined based on [31] as

$$\sigma_{\phi,\mathrm{InSAR}} \approx \frac{1}{2\sqrt{N_L}} \frac{\sqrt{1-\gamma_c^2}}{\gamma_c} \tag{32}$$

$$\sigma_{\phi,\mathrm{MAI}} \approx \frac{1}{\sqrt{N_L}} \frac{\sqrt{1-\gamma_c^2}}{\gamma_c} \tag{33}$$

respectively, where N_L is the effective number of looks for forward- or backward-looking interferograms, and γ_c is the total correlation, which is defined in [41] as

$$\gamma_c = \frac{|\gamma_{\mathrm{spatial,temporal}}|}{1 + \mathrm{SNR}^{-1}} \tag{34}$$

where SNR is the system's signal-to-noise ratio.

The equivalent measurement uncertainty for across- and along-track displacements can be computed by

$$\frac{\lambda_s}{4\pi} \cdot \sigma_{\phi,\mathrm{InSAR}} = \frac{l_s}{2\pi} \cdot \sigma_{\phi,\mathrm{MAI}}. \tag{35}$$

As defined by (32) and (33), the standard deviation of the MAI phase is at least twice as large as the standard deviation of the InSAR phase because of the effective number of looks [31]. Equation (35) can then be rewritten as

$$l_s = \lambda_s/4. \tag{36}$$

Assuming that $n_{\mathrm{dop},f} = \overline{n}_{\mathrm{dop}}$ and $n_{\mathrm{dop},b} = -\overline{n}_{\mathrm{dop}}$, (36) can be rewritten using (22) and (29) as follows:

$$\frac{\lambda}{\sqrt{1 - \frac{\lambda^2}{4\Delta_{\mathrm{az}}^2}\bar{n}_{\mathrm{dop}}^2}} = 2\frac{\Delta_{\mathrm{az}}}{\bar{n}_{\mathrm{dop}}}. \tag{37}$$

To satisfy (36), $\overline{n}_{\mathrm{dop}}$ is

$$\bar{n}_{\mathrm{dop}} = \sqrt{2}\frac{\Delta_{\mathrm{az}}}{\lambda} = \sqrt{2}\frac{V}{\lambda \cdot \mathrm{PRF}}. \tag{38}$$

The Doppler centroid for the equivalent measurement uncertainty can then be defined as

$$\bar{f}_{\mathrm{DC}} = \sqrt{2}\frac{V}{\lambda}. \tag{39}$$

Consequently, the squint angle for equivalent measurement uncertainty $\overline{\gamma}$ is

$$\bar{\gamma} = \sin^{-1}\left(\frac{\sqrt{2}}{2}\right) = \frac{\pi}{4}. \tag{40}$$

This result means that the equivalent measurement uncertainty of the across- and along-track displacements can be achieved using forward- and backward-looking squint angles of 45° and −45°, respectively. With respect to decorrelation and squint angle, theoretical standard deviations of the across- and along-track displacements are shown in Fig. 4. The standard deviation of the along-track displacement is about four times larger than the standard deviation of the across-track displacement when a squint angle of 15° is used; conversely, the standard deviations of the along- and across-track displacements are identical when the squint angle is 45°.

D. Measurement and Uncertainty in 3-D Displacement

Three-dimensional displacement can be retrieved by two InSAR and two MAI phases obtained from two SuperSAR images of ascending and descending pairs [4]. Following the notation given in [19], let $d = (d_x, d_y, d_z)^{\mathbf{T}}$ be the 3-D displacement vector in a local (east, north, up) reference

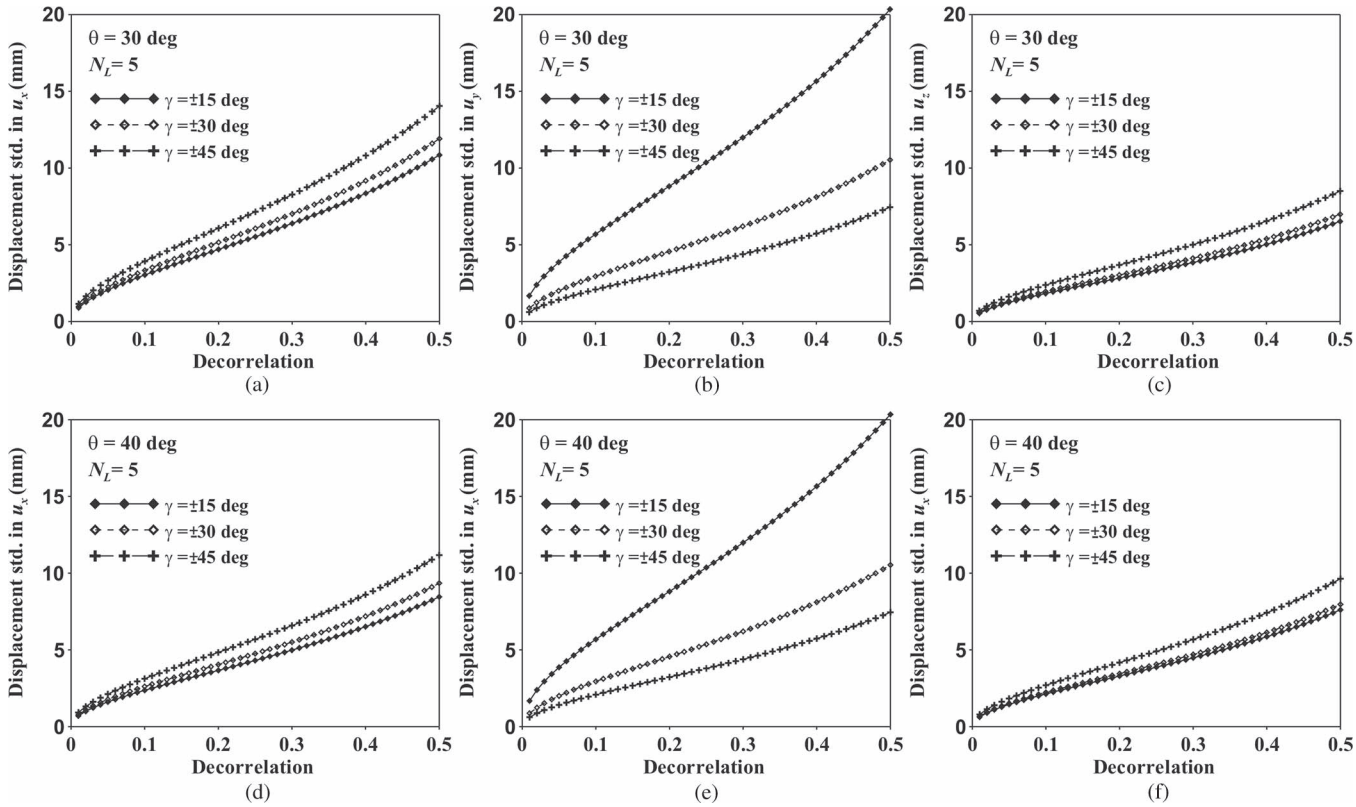

Fig. 5. Variation in the standard deviations of the east, north, and up components of the 3-D displacement with respect to decorrelation using look angles of (a)–(c) 30° and (d)–(f) 40°. For this calculation, system parameters of $V = 7589$ m/s, PRF $= 2300$ Hz, $\lambda = 23.79$ cm, and $\varphi = -10$ and $-170°$ for ascending and descending acquisitions, respectively, are used.

frame and $u = (u_x, u_y, u_z)^{\mathbf{T}}$ be the unit across- or along-track displacement vectors expressed in the same local reference frame. If u is the along-track deformation vector, then $u = (-\sin\alpha, -\cos\alpha, 0)^{\mathbf{T}}$, where α is the satellite track angle north of the across-track vector; if u is the unit across-track deformation vector, then $u = (-\sin\theta \cdot \cos\alpha, \sin\theta \cdot \sin\alpha, \cos\theta)^{\mathbf{T}}$, where θ is the radar incidence from vertical. The deformation r measured from an InSAR or MAI is then given by

$$r = -u^{\mathbf{T}} d. \tag{41}$$

Assuming we produce a total of two InSAR and two MAI observations, we then obtain $R = (r_1, r_2, r_3, r_4)^{\mathbf{T}}$. The weighted least squares solution $(\hat{d}\,)$ for d is defined as follows:

$$\hat{d} = -\left(U^{\mathbf{T}} \mathbf{\Sigma}_R^{-1} U\right)^{-1} \cdot \left(U^{\mathbf{T}} \mathbf{\Sigma}_R^{-1} R\right) \tag{42}$$

where $\mathbf{\Sigma}_R^{-1}$ is the covariance matrix for errors in the observed displacement observations, and U is given by $U = (u_1, u_2, u_3, u_4)^{\mathbf{T}}$. The covariance matrix for the estimated vector components is

$$\mathbf{\Sigma}_d = \left(U^{\mathbf{T}} \mathbf{\Sigma}_R^{-1} U\right)^{-1}. \tag{43}$$

The square root of the diagonal terms of $\mathbf{\Sigma}_d$ gives the standard deviations in the estimates of the east, north, and up components of the 3-D displacement.

Fig. 5 shows the theoretical standard deviation of the 3-D displacement in the east, north, and up directions with respect to both the decorrelation and the squint and look angles. The values in Fig. 5(a)–(f) are calculated from look angles of 30° and 40°, respectively. Parameters of $V = 7589$ m/s, PRF $= 2300$ Hz, $\lambda = 23.79$ cm, and $\alpha = -10$ and $-170°$ for ascending and descending acquisitions, respectively, are used. The parameters are given by the L-band SuperSAR system. The measurement uncertainty for the north component is larger than the measurement uncertainty for the east component when the squint angle is 15°, whereas the measurement uncertainty is smaller for the north than for the east component when the squint angle is 45°, as shown in Fig. 5. Generally, the measurement of the vertical component is more precise than the measurement of the horizontal component. When a squint angle of 30° is imposed, the precision of the vertical component is about 1.7 times more precise than the precision of the horizontal component, whereas the precision values of the east and north components in the horizontal direction are almost identical. The findings mean that a squint angle of 30° is recommended for obtaining the same precision values for the east and north components in polar-orbiting satellites. Moreover, it is not relevant to the radar wavelength because both the across- and along-track displacements are proportional to the wavelength, as known in (20) and (28). Of course, if a shorter wavelength (e.g., X- or C-band) is used for the SuperSAR system, the measurement uncertainty must be lower than L-band. However, expected problems would be temporal decorrelation. Therefore, an L-band SAR sensor would be adequate for the SuperSAR system in order to preserve low temporal decorrelation.

TABLE I
SUPERSAR SYSTEM PARAMETERS USED FOR SIMULATION

Parameters		Values
Pulse Duration Time (μs)		50.0
Chirp Bandwidth (MHz)		35
Sampling Frequency (MHz)		37.1
Pulse Repetition Frequency (Hz)		2300
Carrier Frequency (GHz)		1.260
Effective Azimuth Antenna Dimension (m)		7.0
Satellite's Altitude (km)		550
Satellite's Velocity (m/s)		7589
Look Angle (deg.)		30
Squint Angle (deg.)		30
Track angle (deg.)	Ascending	-10
	Descending	190
Baseline (m)		0

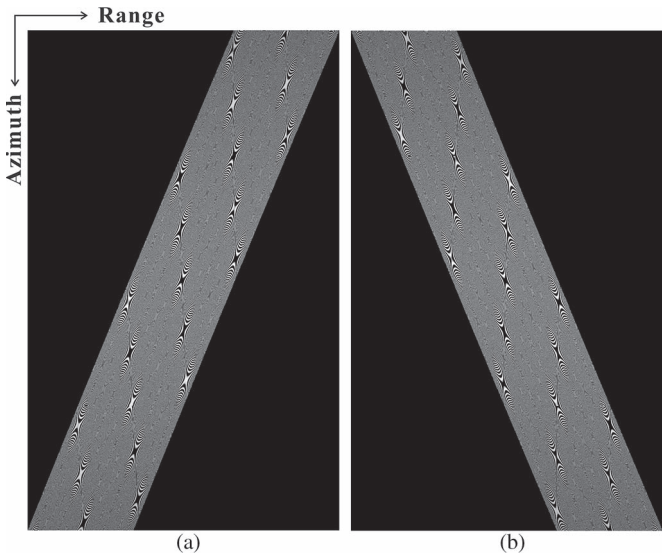

Fig. 6. Simulated SAR raw data for a point target. (a) Forward-looking acquisition. (b) Backward-looking acquisition.

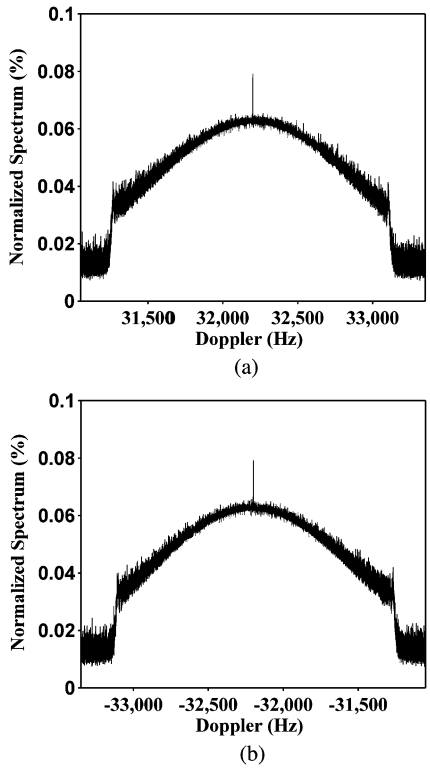

Fig. 7. Normalized spectra of the simulated (a) forward- and (b) backward-looking SAR raw data.

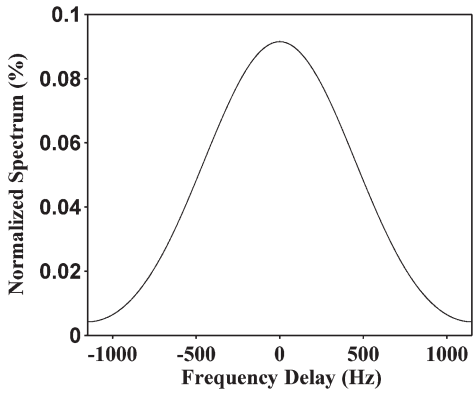

Fig. 8. Ideal case of normalized azimuth spectra for the simulated interferogram.

III. SIMULATION RESULTS

A. Two-Dimensional Displacements

The measurement feasibility of the slant-range displacement in across- and along-track directions has been tested using a simulation of repeat-pass interferometric SuperSAR observations. For this simulation, two forward- and two backward-looking raw signals have been simulated for a static point target. The zero baseline is assumed to simplify the repeat-pass SuperSAR imaging geometry. This simplification means that the flat-Earth and topographic phases on the SuperSAR interferograms can be ignored. Therefore, it can be assumed that the SuperSAR interferometric phase results from surface deformation. The SuperSAR system parameters used in this simulation are listed in Table I. This system can obtain forward- and backward-looking SAR signals from two separate antennas simultaneously.

Fig. 6 shows the simulated forward- and backward-looking SAR raw data for a point target. The pixel sizes of the simulated raw signals in the azimuth and range directions are 8780 and 5474, respectively. The range time delay between the first and last azimuth lines for one target reaches about 3620 pixels because of the large squint imaging geometry. The conventional SAR focusing algorithm cannot be applied to an unmodified high-squint-mode SAR system because this algorithm uses some approximations. Although the conventional algorithm is used, serious image degradation (such as defocusing) would

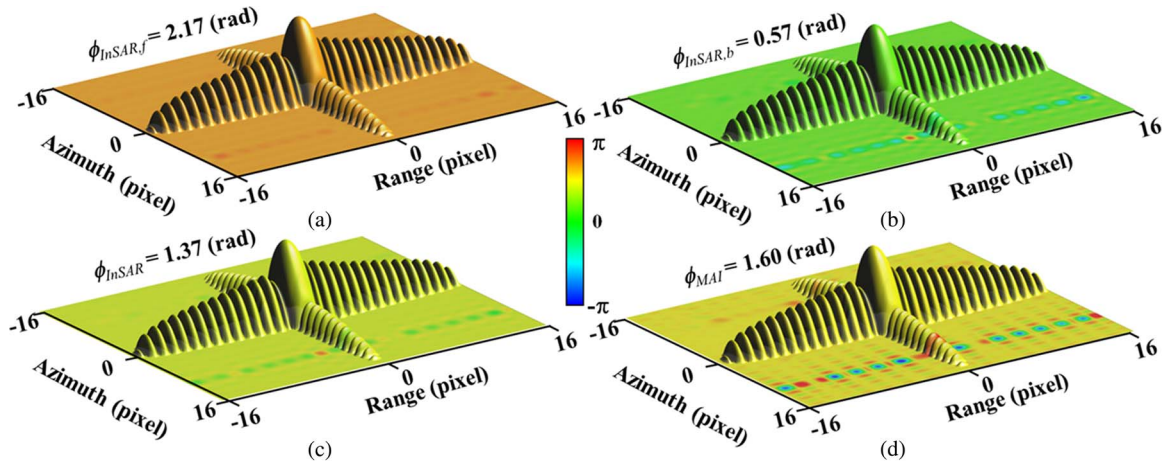

Fig. 9. Simulated interferograms. (a) and (b) Forward- and backward-looking interferograms. (c) InSAR interferogram. (d) MAI interferogram. Across- and along-track displacements of 3 cm are applied to this simulation.

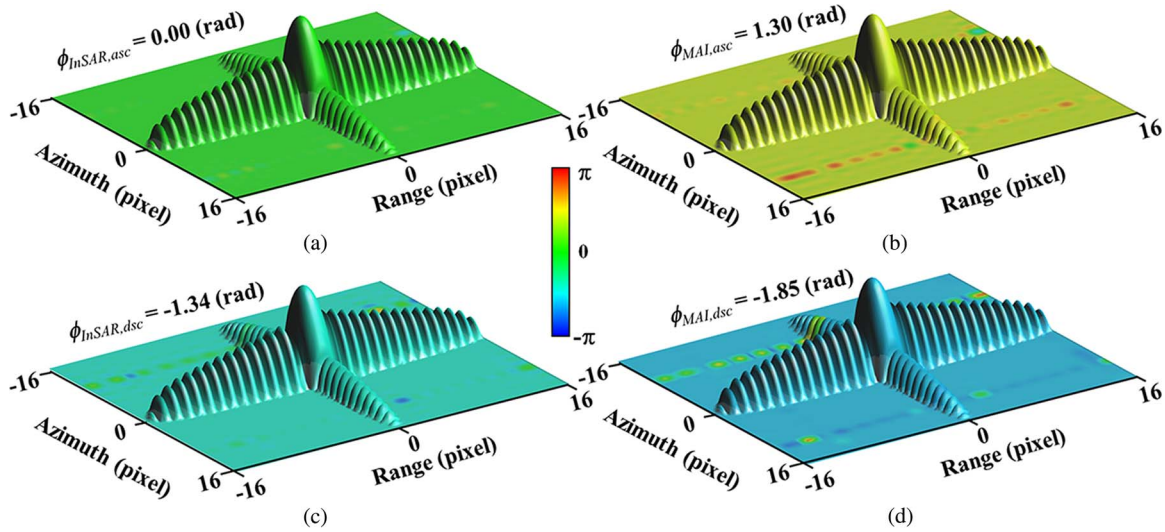

Fig. 10. Simulated interferograms. InSAR and MAI interferograms of (a) and (b) ascending orbit acquisitions (track angle of $-10°$) and (c) and (d) descending orbit acquisitions (track angle of 190°). Ground surface displacements of 3, 3, and 2 cm in the east, north, and up directions are used for this simulation.

occur. This issue results from higher order range–azimuth coupling terms and can be corrected using nonlinear frequency modulation filtering or pulse methods [39]. The Doppler centroids of the simulated forward- and backward-looking SAR data are 32 200 and $-32\,200$ Hz, respectively (see Fig. 7). Because the forward- and backward-looking single-look complex (SLC) images are created from different portions of the Doppler spectra, we cannot generate an interferogram from the SLC images because these images do not have correlated spectral contributions. However, the forward- and backward-looking interferograms can be created from the forward- and backward-looking repeat-pass interferometric pairs, respectively, only if the interferometric pairs can preserve the correlated spectra. These interferograms can be defined by the cross correlation in the frequency domain between the master and slave SLC images because these interferograms are created using complex conjugate multiplication of the master SLC image with the slave SLC image. This methodology means that the Fourier transform of an interferogram is defined as a function of the frequency shift. Therefore, the forward- and backward-looking interferograms can preserve the correlated spectra, as shown in Fig. 8.

The InSAR interferogram is produced by multiplying the forward- and backward-looking interferograms, and the MAI interferogram is produced using complex conjugate multiplication of the forward-looking interferogram with the backward-looking interferogram. Consequently, the InSAR and MAI interferograms can be defined by convolution and cross correlation in the frequency domain between the forward- and backward-looking interferograms, respectively. Because the forward- and backward-looking interferograms can have the aforementioned correlated spectral contributions, we can create coherent InSAR and MAI interferograms from the SuperSAR images.

We have simulated four sets of SAR raw data for a point object that has displacements of 3 cm in both the across- and

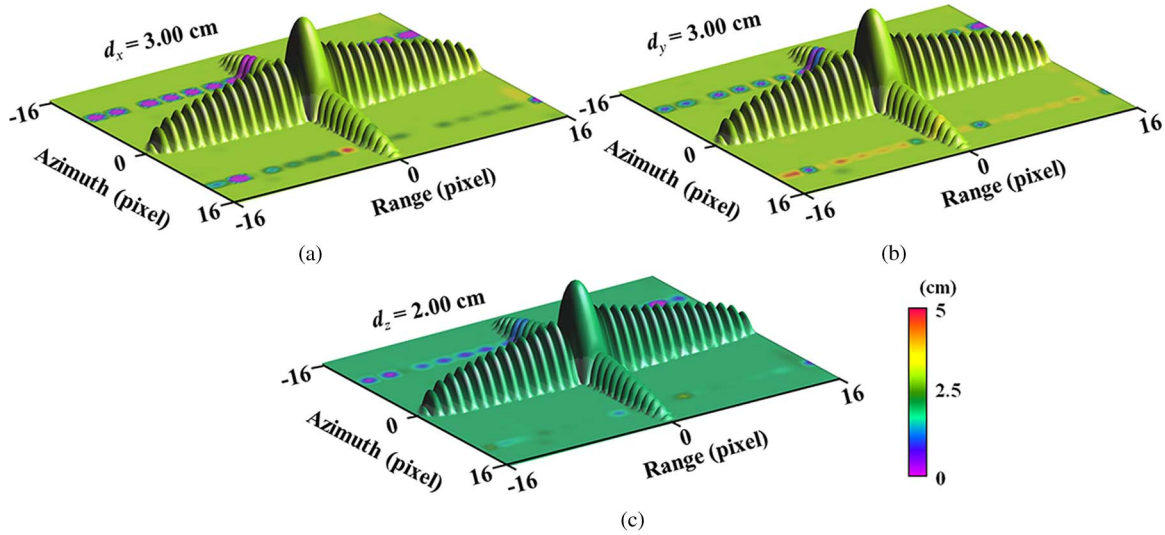

Fig. 11. Ground displacement estimated from the simulated interferograms. (a) East component. (b) North component. (c) Up component.

along-track directions. The four SAR raw data sets are two forward- and two backward-looking SLC images acquired from the master and slave observations, respectively. These simulations are conducted using the SuperSAR system parameters (see Table I). Fig. 9(a) and (b) presents the simulated forward- and backward-looking interferograms, respectively, and Fig. 9(c) and (d) displays InSAR and MAI interferograms estimated from the forward- and backward-looking interferograms of Fig. 9(a) and (b), respectively. The adjusted radar wavelength and azimuth antenna lengths are about 27.56 and 11.78 cm, which are calculated from (22) and (29), respectively. The displacement-induced phases of forward- and backward-looking interferograms are about 2.17 and 0.57 rad, respectively. These phase values correspond to about 4.75 and 1.25 cm in forward- and backward-looking LOS directions, respectively. The InSAR and MAI interferometric phases are about 1.37 and 1.60 rad, respectively, and correspond to 3.0 cm in both the across- and along-track displacements, respectively. This correspondence means that the SuperSAR imaging system, which is the forward- and backward-looking squint-mode SAR system, can precisely measure the 2-D displacement from the integration of the InSAR and MAI methods. Assuming that the interferometric coherence is about 0.8, the theoretical measurement precision values from (30) and (31) are about 3.67 and 6.35 mm in the across- and along-track directions, respectively, when there are five effective looks. These precision values might be further improved by a factor of about 2 in both the across- and along-track directions, respectively, when an adaptive filter, such as the Goldstein filter [42], is applied. This result indicates that the SuperSAR imaging system could enable us to measure the 2-D surface displacement with subcentimeter precision.

B. Three-Dimensional Displacements

The measurement feasibility of the 3-D displacement has been tested using the simulation of repeat-pass interferometric SuperSAR observations from ascending and descending orbits. Four SAR raw data sets for the ascending and descending orbit acquisitions have been simulated. Track angles of -10° and 190° are used for the ascending and descending orbit acquisitions, respectively (see Table I). The east (dx), north (dy), and up (dz) components of 3-D displacement used for the simulation are 3.0, 3.0, and 2.0 cm, respectively. Two InSAR and two MAI interferograms are simulated from the eight SAR raw data sets and are used to determine the east, north, and up components of the 3-D displacement vector using (42). Fig. 10 presents two InSAR and two MAI interferograms created from eight simulated SAR raw data sets. The estimated ascending InSAR and MAI phases are about 0.00 and 1.30 rad, respectively. These phases correspond to about 0.00 and 2.43 cm in the across- and along-track directions, respectively. The estimated descending InSAR and MAI phases are about -1.34 and -1.85 rad, respectively. These phases correspond to about -2.95 and -3.48 cm in the across- and along-track directions of the descending orbit acquisition, respectively. Fig. 11 shows the east, north, and up components of the 3-D displacement vector determined from the integration of the ascending and descending InSAR and MAI observations. The east, north, and up components of the estimated 3-D displacement are 3.00, 3.00, and 2.00 cm, respectively. Assuming that the interferometric coherence is about 0.8, the theoretical measurement precision values of the 3-D displacement are about 4.05, 4.56, and 3.45 mm in the east, north, and up directions, respectively, when there are five effective looks. The precision of the vertical component is better than the precision of the horizontal component, but the precision values of the horizontal component are quite similar in the east and north directions. The precision values might be further improved in all directions if an adaptive filter, such as the Goldstein filter, is applied. Moreover, it is noted that the weighted least square adjustment for the 3-D displacement measurement may not be necessary because the measurement precision values in the across- and along-track directions are very similar to each other. The results indicate that the SuperSAR imaging system might enable us to measure the 3-D surface displacement in all directions (east, north, and up) with subcentimeter precision.

IV. Conclusion

The MAI method has recently been developed, and this method achieves a remarkable improvement in along-track displacement measurements. This method can measure the along-track displacement with measurement accuracy of several centimeters. Despite the remarkable improvement resulting from the MAI technique, the measurement uncertainty of the along-track displacement is a few centimeters, which is almost ten times lower than the measurement uncertainty of the LOS displacement. Because of this difference between measurement accuracy values for the along-track and LOS displacements, it is difficult to perfectly retrieve information regarding 3-D surface deformation. To surmount this limitation, the SuperSAR imaging system has been proposed, and this system is a novel multi-azimuth SAR system that is capable of detecting Earth surface deformation in three dimensions.

In this paper, we investigate the feasibility of precise 3-D surface displacement measurement from the SuperSAR imaging system using a point target simulation. First, from the mathematical derivations of the SuperSAR measurements, we establish a relationship between the InSAR phase and the across-track displacement and a relationship between the MAI phase and the along-track displacement from the SuperSAR imaging geometry. Moreover, the theoretical uncertainties of the SuperSAR measurement are analyzed in the across- and along-track directions, and the theoretical accuracy of 3-D displacement measurement from the SuperSAR system is also investigated with respect to both the decorrelation and the squint and look angles. Assuming that the interferometric coherence is about 0.8 and that there are five effective looks, the theoretical 2-D measurement precision values are about 3.67 and 6.35 mm in the across- and along-track directions, respectively, and the theoretical 3-D measurement precision values of the 3-D displacement are about 4.05, 4.56, and 3.45 mm in the east, north, and up directions, respectively. This result proves that the SuperSAR imaging system is capable of measuring the 3-D surface displacement in all directions with subcentimeter precision.

References

[1] G. Feng *et al.*, "Calibration of an InSAR-derived coseismic deformation map associated with the 2011 Mw-9.0 Tohoku-Oki earthquake," *IEEE Geosci. Remote Sens. Lett.*, vol. 9, no. 2, pp. 302–306, Mar. 2012.

[2] J. Hu *et al.*, "3D coseismic displacement of 2010 Darfield, New Zealand earthquake estimated from multi-aperture InSAR and D-InSAR measurements," *J. Geod.*, vol. 86, no. 11, pp. 1029–1041, 2012.

[3] T. J. Wright, J. R. Elliott, H. Wang, and I. Ryder, "Earthquake cycle deformation and the Moho: Implications for the rheology of continental lithosphere," *Tectophysics*, vol. 609, pp. 504–523, 2013.

[4] H.-S. Jung, Z. Lu, J. S. Won, M. P. Poland, and A. Miklius, "Mapping three-dimensional surface deformation by combining multiple-aperture interferometry and conventional interferometry: Application to the June 2007 eruption of Kilauea volcano, Hawaii," *IEEE Geosci. Remote Sens. Lett.*, vol. 8, no. 1, pp. 34–38, Jan. 2011.

[5] Z. Lu, D. Dzurisin, J. Biggs, C. Wicks, Jr., and S. McNutt, "Ground surface deformation patterns, magma supply, and magma storage at Okmok volcano, Alaska, inferred from InSAR analysis: 1. Inter-eruptive deformation, 1997–2008," *J. Geophys. Res.*, vol. 115, 2010, Art. ID. B00B03.

[6] C.-W. Lee, Z. Lu, J.-S. Won, H.-S. Jung, and D. Dzurisin, "Dynamic deformation of Seguam Island, Alaska, 1992–2008, from multi-interferogram InSAR processing," *J. Volcanol. Geothermal Res.*, vol. 260, pp. 43–51, 2013.

[7] P. Lundgren *et al.*, "Evolution of dike opening during the March 2011 Kamoamoa fissure eruption, Kīlauea Volcano, Hawaii," *J. Geophy. Res.*, vol. 118, pp. 897–914, 2013.

[8] M.-J. Jo *et al.*, "Measurement of slow-moving along-track displacement from an efficient multiple-aperture SAR interferometry (MAI) stacking," *J. Geod.*, vol. 89, no. 5, pp. 411–425, 2015.

[9] D. Tarchi *et al.*, "Landslide monitoring by using ground-based SAR interferometry: An example of application to the Tessina landslide in Italy," *Eng. Geol.*, vol. 68, no. 1/2, pp. 15–30, Feb. 2003.

[10] M. Crosetto *et al.*, "Interferometric SAR monitoring of the Vallcebre landslide (Spain) using corner reflectors," *Nat. Hazards Earth Syst. Sci.*, vol. 13, pp. 923–933, 2013.

[11] C. Zhao, Z. Lu, Q. Zhang, and J. Fuente, "Large area landslide detection and monitoring with ALOS/PALSAR imagery data over Northern California and Southern Oregon, USA," *Remote Sens. Env.*, vol. 124, pp. 348–359, 2012.

[12] C. Zhao, Z. Lu, and Q. Zhang, "Time-series deformation monitoring over mining regions with SAR intensity-based offset measurements," *Remote Sens. Lett.*, vol. 4, no. 5, pp. 436–445, 2013.

[13] H. C. Jung, S.-W. Kim, H.-S. Jung, K. D. Min, and J.-S. Won, "Satellite observation of coal mining subsidence by persistent scatterer analysis," *Eng. Geol.*, vol. 92, no. 1/2, pp. 1–13, 2007.

[14] L. Zhang *et al.*, "Mapping ground surface deformation using temporarily coherent point SAR interferometry: Application to Los Angeles Basin," *Remote Sens. Environ.*, vol. 117, pp. 429–439, Feb. 2012.

[15] J.-K. Choi *et al.*, "Integration of GIS and SAR interferometry for a coal mine subsidence hazard map in Taebaek, Korea," *Int. J. Remote Sens.*, vol. 32, no. 23, pp. 8161–8181, Dec. 2011.

[16] M. McMillan *et al.*, "Mapping ice-shelf flow with interferometric synthetic aperture radar stacking," *J. Glaciol.*, vol. 58, no. 208, pp. 277–289, Jan. 2012.

[17] J. J. Sharma, I. Hajnsek, K. P. Papathanassiou, and A. Moreira, "Estimation of glacier ice extinction using long-wavelength airborne pol-InSAR," *IEEE Trans. Geosci. Remote Sens.*, vol. 51, no. 6, pp. 3715–3732, Jun. 2013.

[18] J. W. Park *et al.*, "Sustained retreat of the Pine Island Glacier," *Geophys. Res. Lett.*, vol. 40, pp. 2137–2142, May 2013.

[19] T. J. Wright, B. E. Parsons, and Z. Lu, "Toward mapping surface deformation in three dimensions using InSAR," *Geophys. Res. Lett.*, vol. 31, no. 1, Jan. 2004, Art. ID. L01607.

[20] Y. Fialko, D. Sandwell, M. Simons, and P. Rosen, "Three-dimensional deformation caused by the Bam, Iran, earthquake and the origin of shallow slip deficit," *Nature*, vol. 435, pp. 295–299, 2005.

[21] D. Raucoulesa, M. de Michelea, J.-P. Maletb, and P. Ulrichb, "Time-variable 3D ground displacements from high-resolution synthetic aperture radar (SAR). Application to La Valette landslide (South French Alps)," *Remote Sens. Env.*, vol. 139, pp. 198–204, 2013.

[22] G. J. Funning, B. Parsons, T. J. Wright, J. A. Jackson, and E. J. Fielding, "Surface displacements and source parameters of the 2003 Bam, Iran earthquake from Envisat advanced synthetic aperture radar imagery," *J. Geophys. Res.*, vol. 110, no. B9, 2005, Art. ID. B0940.

[23] E. Erten, A. Reigberb, and O. Hellwicha, "Generation of three-dimensional deformation maps from InSAR data using spectral diversity techniques," *ISPRS J. Photogramm. Remote Sens.*, vol. 64, no. 4, pp. 388–394, Jul. 2010.

[24] L. Gray, "Using multiple RADARSAT InSAR pairs to estimate a full three-dimensional solution for glacial ice movement," *Geophys. Res. Lett.*, vol. 38, no. 5, Mar. 2011, Art. ID. L05502.

[25] S. Gudmundsson, F. Sigmundsson, and J. Carstensen, "Three-dimensional surface motion maps estimated from combined interferometric synthetic aperture radar and GPS data," *J. Geophys. Res.*, vol. 107, no. B10, pp. 2250–2264, 2002.

[26] S. Samsonov, K. Tiampo, J. Rundle, and Z. H. Li, "Application of DInSAR-GPS optimization for derivation of fine-scale surface motion maps of Southern California," *IEEE Trans. Geosci. Remote Sens.*, vol. 45, no. 2, pp. 512–521, Feb. 2007.

[27] F. Guglielmino, G. Nunnari, G. Puglisi, and A. Spata, "Simultaneous and integrated strain tensor estimation from geodetic and satellite deformation measurements to obtain three-dimensional displacement maps," *IEEE Trans. Geosci. Remote Sens.*, vol. 49, no. 6, pp. 1815–1826, Jun. 2011.

[28] J. Hu, Z. W. Li, Q. Sun, J. J. Zhu, and X. L. Ding, "Three-dimensional surface displacements from InSAR and GPS measurements with variance component estimation," *IEEE Geosci. Remote Sens. Lett.*, vol. 9, no. 4, pp. 754–758, Jul. 2012.

[29] J. Hu *et al.*, "Resolving three dimensional surface displacements from InSAR measurements: A review," *Earth-Sci. Rev.*, vol. 133, pp. 1–17, Jun. 2014.

[30] N. B. D. Bechor and H. A. Zebker, "Measuring two-dimensional movements using a single InSAR pair," *Geophys. Res. Lett.*, vol. 33, no. 16, Aug. 2006, Art. ID. L16311.

[31] H.-S. Jung, J.-S. Won, and S.-W. Kim, "An improvement of the performance of multiple aperture SAR interferometry (MAI)," *IEEE Trans. Geosci. Remote Sens.*, vol. 47, no. 8, pp. 2859–2869, Aug. 2009.
[32] H.-S. Jung, Z. Lu, and L. Zhang, "Feasibility of along-track displacement measurement from Sentinel-1 interferometric wide-swath mode," *IEEE Trans. Geosci. Remote Sens.*, vol. 51, no. 1, pp. 573–578, Jan. 2013.
[33] H.-S. Jung, W.-J. Lee, and L. Zhang, "Theoretical accuracy of along-track displacement measurements from multiple-aperture interferometry (MAI)," *Sensors*, vol. 14, no. 9, pp. 17703–17724, Sep. 2014.
[34] H.-S. Jung, D.-T. Lee, Z. Lu, and J.-S. Won, "Ionospheric correction of SAR interferograms by multiple-aperture interferometry," *IEEE Trans. Geosci. Remote Sens.*, vol. 51, no. 5, pp. 3191–3199, May 2013.
[35] Z. Liu, H.-S. Jung, and Z. Lu, "Joint correction of ionosphere noise and orbital error in L-band SAR interferometry of interseismic deformation in southern California," *IEEE Trans. Geosci. Remote Sens.*, vol. 52, no. 6, pp. 3421–3427, Jun. 2014.
[36] A. Shepherd and the SuperSAR team, "SuperSAR: A mission to detect earth surface deformation in three dimensions from a single satellite platform," presented at the Eur. Geosciences Union, Vienna, Austria, Apr. 2010, Paper EGU2010-2764.
[37] T. Wright, M. Garthwaite, H.-S. Jung, and A. Shepherd, "How accurately can current and future InSAR missions map tectonic strain?" in *Proc. Fringe*, Sep. 2011, pp. 1–43.
[38] R. K. Raney, H. Runge, R. Bamler, I. G. Cumming, and F. H. Wong, "Precision SAR processing using chirp scaling," *IEEE Trans. Geosci. Remote Sens.*, vol. 32, no. 4, pp. 786–799, Jul. 1994.
[39] G. W. Davison, I. G. Cumming, and M. R. Ito, "A chirp scaling approach for processing squint mode SAR data," *IEEE Trans. Aerosp. Electron. Syst.*, vol. 32, no. 1, pp. 121–133, Jan. 1996.
[40] D. T. Sandwell and E. J. Price, "Phase gradient approach to stacking interferograms," *J. Geophys. Res.*, vol. 103, no. B12, pp. 30 183–30 204, 1998.
[41] H. A. Zebker and J. Villasenor, "Decorrelation in interferometric radar echoes," *IEEE Trans. Geosci. Remote Sens.*, vol. 30, no. 5, pp. 950–959, Sep. 1992.
[42] R. M. Goldstein and C. L. Werner, "Radar interferogram filtering for geophysical application," *Geophys. Res. Lett.*, vol. 25, no. 21, pp. 4035–3048, 1998.

Hyung-Sup Jung (M'09) received the M.S. and Ph.D. degrees in geophysics and remote sensing from Yonsei University, Seoul, Korea, in 1998 and 2007, respectively.

He is currently an Associate Professor with the Department of Geoinfomatics, The University of Seoul, Seoul. His primary research interests include developments of synthetic aperture radar (SAR), interferometric SAR (InSAR), multiple-aperture InSAR (MAI) and small baseline subset (SBAS) InSAR processors, and algorithms related to 3-D deformation mapping by combining MAI and InSAR and 2-D surface velocity estimation by combining MAI and along-track interferometry.

Zhong Lu received the B.S. and M.S. degrees from Peking University, Beijing, China, in 1989 and 1992, respectively, and the Ph.D. degree from the University of Alaska Fairbanks, Fairbanks, AK, USA, in 1996. He was a Physical Scientist with U.S. Geological Survey (USGS) during 1997–2013 and is now a Professor and Shuler-Foscue Endowed Chair at the Huffington Department of Earth Sciences, Southern Methodist University, Dallas, TX, USA. He is a Principal Investigator of projects funded by the National Aeronautics and Space Administration, European Space Agency, Japan Aerospace Exploration Agency, German Aerospace Agency, and USGS on the study of land surface deformation using satellite interferometric synthetic aperture radar (SAR) (InSAR) imagery. He has produced more than 45 lead-authored and 75 coauthored peer-reviewed journal articles and book chapters focused on InSAR techniques and applications. He is the coauthor of the book *InSAR Imaging of Aleutian Volcanoes: Monitoring a Volcanic Arc From Space* (Springer, 2014). His research interests include technique developments of SAR, InSAR, and persistent scatterer InSAR processing and their applications on natural hazard monitoring and natural resource management.

Andrew Shepherd received the B.Sc. degree in physics with astrophysics and the Ph.D. degree in physics from the University of Leicester, Leicester, U.K.

He is currently a Professor of Earth observation at the University of Leeds, Leeds, U.K., Director of the NERC Centre for Polar Observation and Modelling, Principal Scientific Advisor to the European Space Agency (ESA) CryoSat satellite mission, and co-leader of the ESA–NASA Ice Sheet Mass Balance Inter-comparison Exercise. He uses satellites to study physical processes of Earth's climate, and his main contributions to science have involved developing remote observations of the cryosphere, with particular emphasis on the quantitative techniques of radar interferometry and radar altimetry. He has also worked on studies of arid land degradation using satellite infrared radiometry and models of atmospheric radiative transfer, and he has led satellite validation campaigns in Europe, Africa, and Antarctica. He has held academic posts at the University College London, London, U.K., at the University of Cambridge, Cambridge, U.K., and at the University of Edinburgh, Edinburgh, U.K.

Tim Wright received the B.A. degree in natural sciences from the University of Cambridge, Cambridge, U.K., in 1995, the M.Sc. in remote sensing from the University of London, London, U.K., in 1997, and the D.Phil. degree in satellite geodesy from the University of Oxford, Oxford, U.K., in 2000.

He is currently a Professor of satellite geodesy at the University of Leeds, Leeds, U.K., and the Director of the NERC Centre for the Observation and Modelling of Earthquakes, Volcanoes and Tectonics. His work has been at the forefront of developing the use of satellite radar interferometry (InSAR) for measuring tectonic and volcanic deformation. His achievements include the first demonstration that interseismic strain can be measured using InSAR; the investigation of a series of major earthquakes using geodesy, seismology, and geomorphology; and the mapping and modelling of a major rifting episode in Afar, Ethiopia. He led the NERC-funded Afar Rift Consortium and co-leads LICS, a NERC large Grant to "Look Inside the Continents from Space." He has published more than 65 papers in major international journals, and his work is highly cited.

Prof. Wright was a recipient of the AGU Geodesy Section Award in 2014 and the Rosenstiel Award from the University of Miami in 2015. He was also the British Geophysical Association's Bullerwell Lecturer in 2015.